

Effect of Triangularity on Ion-Temperature-Gradient-Driven Turbulence

J.M. Duff,^{1, a)} B.J. Faber,¹ C.C. Hegna,¹ M.J. Pueschel,^{2,3} and P.W. Terry¹

¹⁾*University of Wisconsin-Madison, Madison WI, 53706, USA*

²⁾*Dutch Institute for Fundamental Energy Research, 5612 AJ Eindhoven,
The Netherlands*

³⁾*Eindhoven University of Technology, 5600 MB Eindhoven,
The Netherlands*

The linear and nonlinear properties of ion-temperature-gradient-driven (ITG) turbulence with adiabatic electrons are modeled for axisymmetric configurations for a broad range of triangularities δ , both negative and positive. Peak linear growth rates decrease with negative δ but increase and shift toward a finite radial wavenumber k_x with positive δ . The growth-rate spectrum broadens as a function of k_x with negative δ and significantly narrows with positive δ . The effect of triangularity on linear instability properties can be explained through its impact on magnetic polarization and curvature. Nonlinear heat flux is weakly dependent on triangularity for $|\delta| \leq 0.5$, decreasing significantly with extreme δ , regardless of sign. Zonal modes play an important role in nonlinear saturation in the configurations studied, and artificially suppressing zonal modes increased nonlinear heat flux by a factor of about four for negative δ , increasing with positive δ by almost a factor of 20. Proxies for zonal-flow damping and drive suggest that zonal flows are enhanced with increasing positive δ .

^{a)}Electronic mail: jduff2@wisc.edu.

I. INTRODUCTION

Ion-scale drift-wave-driven turbulence is considered to be an important source of heat and particle transport in fusion experiments¹. Although plasma shaping is known to substantially impact magnetohydrodynamic (MHD) stability properties², there is no complete picture of how plasma shaping affects drift-wave-driven turbulence. For axisymmetric configurations, larger values of elongation κ , a parameterization of how ellipsoidal the cross-section of a magnetic flux surface is in the vertical direction, is known to have a stabilizing effect on ion temperature gradient (ITG)^{3,4} and trapped electron (TEM)⁵ drift-wave modes^{6–8}. The effect of the triangularity δ —particularly negative triangularity—of axisymmetric configurations on drift-wave-driven turbulence is not fully understood. The present work seeks to understand the physics of changes to confinement produced by negative triangularity by studying an ITG turbulence regime, where saturation mechanisms are well-understood, include extremes in triangularity as a first assessment of whether the common approach of focusing on moderate values of δ may overlook interesting and potentially beneficial regimes, and determine if and when (quasi-)linear physics cannot capture nonlinear trends, potentially revealing changes to saturation efficiency.

The DIII-D and TCV experiments have explored negative triangularity configurations, achieving improved confinement and lower fluctuation levels relative to their positive triangularity counterparts^{9–14}. These observations have been reproduced in gyrokinetic and gyrofluid simulations^{14–19}. The largest range of triangularities studied in the experiments was $-0.65 \leq \delta_{\text{LCFS}} \leq 0.55$ at the last closed flux surface (LCFS)¹¹, the drift-wave stability properties of which were studied in Ref.¹⁷. Recent studies based on linear and nonlinear simulations commonly compare equilibria similar to the experimental regimes, with $|\delta_{\text{LCFS}}| \lesssim 0.4$ ^{16–18}. In the present work, a broader range of triangularities is pursued to enable identification of possible new turbulence regimes. Note that experimental scenarios of $\delta = 0.8$ and $\delta = -0.9$ have been considered in the past²⁰, and TCV is designed for $-0.7 \leq \delta \leq 1$ ²¹. These linear and nonlinear simulations focused on TEM-dominant regimes, however ITGs were also present.

Linear electrostatic gyrokinetic studies have found positive triangularity to be marginally destabilizing for ITGs at low elongation (typically $1 \leq \kappa \lesssim 1.5$), but marginally stabilizing at high elongation^{8,22}. Previous nonlinear electrostatic gyrokinetic simulations showed nonlinear heat diffusivities followed linear stability trends, however triangularity is written as a function of elongation as represented in parameterized JET equilibrium data²², where elongation is well known to have a stabilizing effect^{6–8}. In Refs.^{6,23}, the effect of δ was separated from the effect of κ on ITG-

dominated turbulence, where nonlinear gyrokinetic simulations suggest $\delta < 0$ (> 0) is marginally (de)stabilizing, with more pronounced (de)stabilization at larger elongation^{6,23}. In Ref.⁶, triangularity was varied $-0.5 \leq \delta \leq 0.75$, holding κ constant, and Ref.²³ studied flux surfaces with $\delta = \pm 0.2$. In both studies ITGs were the dominant linear instability and heat flux increased with δ , however, unstable TEMs were present as well, and Ref.⁶ attributed the increased heat fluxes for $\delta > 0$ to the destabilization of low-wavenumber TEMs. This complication does not arise in the present work due to the use of the adiabatic-electron approximation.

While high-fidelity gyrokinetic simulations typically require kinetic electrons, the adiabatic-electron approximation has been used successfully to replace kinetic electrons in scenarios with low density gradients²⁴. Nonlinear ITG turbulence with adiabatic electrons has been studied in the context of optimizing a global equilibrium to reduce heat loss due to turbulence, where the optimized equilibrium had a triangularity of $\delta = -0.625$ ²⁵. Although the findings of Ref.²⁵ indicate strong negative triangularity reduces turbulent transport in ITG turbulence with adiabatic electrons, the triangularity was not allowed to drop below $\delta \approx -0.65$.

Previous studies have attempted to explain the effect of triangularity on turbulence through geometric quantities. Some suggest local changes in driving gradients via $(\partial_r \psi)^{-1} \nabla \psi$ at fixed background temperature gradient, where ψ is a poloidal flux function and r the minor radial coordinate^{9,10}. Other works have suggested local shear is responsible^{8,26}. However, changing the shaping of a flux surface changes both $(\partial_r \psi)^{-1} \nabla \psi$ and local shear in addition to the curvature vector, an instability drive mechanism for ITGs. The present work provides insight into the impact of finite perpendicular wavenumber k_\perp (which includes information from local shear and $(\partial_r \psi)^{-1} \nabla \psi$) and curvature on linear mode structure.

Turbulent transport of a magnetic configuration is often estimated using linear quantities with a quasilinear mixing-length argument. Typically, the quasilinear heat diffusivities are estimated from random-walk scalings: $\chi \sim \sum_{k_\perp} \gamma / \langle k_\perp^2 \rangle$, where γ is a linear growth rate at a given perpendicular wavenumber k_\perp , and the eigenmode average for some quantity A is defined as $\langle A \rangle = \int d\Theta A |\Phi|^2 / \int d\Theta |\Phi|^2$, with Φ being the electrostatic potential and Θ the coordinate along the field line assuming a ballooning-like ansatz^{27,28}. Quasilinear transport models can provide good predictions for turbulence-induced transport in tokamaks^{29–33}. However, traditional quasilinear models break down and fail to predict nonlinear behavior for certain magnetic configurations³⁴, when close to critical gradients^{35–37}, or when the ratio of plasma pressure to magnetic field pressure β is varied^{38–41}. The present work seeks to evaluate the capability of the quasilinear model to capture the nonlinear behavior for configurations with a wide range of triangularities.

It is well known that zonal flows play a prominent role in the nonlinear saturation of ITG turbulence in tokamaks^{35,42,43}. Zonal flows provide saturation mechanisms through flow shear⁴⁴, by mediating energy transfer from unstable to stable modes, or by providing a direct energy sink through collisional dissipation^{45–51}. The simulations presented in this work confirm zonal modes play a major role in nonlinear saturation of ITG turbulence, and that the zonal flows may be enhanced in geometries with increasing positive triangularity.

In Sec. II, the models used to generate local MHD equilibrium solutions with prescribed axisymmetric shaping are presented along with key geometric quantities associated with ITG damping and drive. In Sec. III, results from linear gyrokinetic simulations are presented, showing how the growth-rate spectrum changes with triangularity and how key geometric quantities influence these changes. Section IV describes a quasilinear transport model in detail and presents nonlinear gyrokinetic heat fluxes and comparisons to the quasilinear model predictions as a function of triangularity, followed by an analysis of zonal-flow impact. Results are summarized in Sec. V.

II. MODEL

In the present work, solutions to the MHD equilibrium are required local to a magnetic surface. Following Ref.⁵², local solutions to the Grad-Shafranov equation can be found that are parameterized by a small number of important geometry quantities such as triangularity. A local equilibrium is a specification of magnetic coordinates near a single flux surface that satisfy the MHD force balance equation $\mathbf{J} \times \mathbf{B} = \nabla p$ and quasineutrality $\nabla \cdot \mathbf{J} = 0$ consistently with Ampère's Law $\nabla \times \mathbf{B} = \mu_0 \mathbf{J}$. Consistent with MHD equilibrium conditions, the components of the magnetic field and current normal to the flux surface must vanish. Generating a local MHD equilibrium solution requires specifying an inverse mapping of the surface in straight-field-line coordinates (or, equivalently, the poloidal magnetic field strength in axisymmetric configurations), the safety factor q , and two of three flux surface quantities: the flux-surface-averaged parallel current, flux-surface-averaged local shear $q' = dq/d\psi$, and pressure gradient $p' = dp/d\psi$ ⁵³. With straight-field-line coordinates, the divergence-free form of the magnetic field is $\mathbf{B} = \nabla\psi \times \nabla(q\Theta - \zeta)$, so that $\mathbf{B} \cdot \nabla\psi = 0$, where ζ is chosen to be the geometric toroidal angle and Θ is the straight-field-line poloidal angle.

The effects of triangularity and elongation on axisymmetric shaping can be introduced following the Miller formulation⁵². Near a flux surface with finite elongation κ and triangularity δ , the major radius R and height of the flux surface Z are parameterized by the geometric poloidal angle

θ as

$$R = R_0 + r \cos[\theta + \arcsin \delta \sin \theta], \quad (1)$$

$$Z = \kappa r \sin \theta. \quad (2)$$

The Miller equilibrium writes the magnetic field for a flux surface labeled by poloidal flux $\psi = \psi_0$ in cylindrical coordinates $\mathbf{B} = \nabla\psi \times \nabla\zeta + f(\psi_0)\nabla\zeta$. The magnetic field components are $f(\psi_0) = RB_r$ and

$$B_p = \frac{\partial_r \psi [\sin^2(\theta + x \sin \theta)(1 + x \cos \theta)^2 + \kappa^2 \cos^2 \theta]^{1/2}}{\kappa R \{ \cos(x \sin \theta) + \partial_r R_0 \cos \theta + (s_\kappa - s_\delta \cos \theta + [1 + s_\kappa]x \cos \theta) \sin \theta \sin(\theta + x \sin \theta) \}}, \quad (3)$$

$$s_\kappa = \frac{r}{\kappa} \frac{\partial \kappa}{\partial r}, \quad (4)$$

$$s_\delta = \frac{r}{\sqrt{1 - \delta^2}} \frac{\partial \delta}{\partial r}, \quad (5)$$

where $\delta = \sin x$, and $\partial_r \psi$ is determined through $q = d\Psi/d\psi$, where Ψ is a toroidal flux function. The equilibrium is fully described with $\hat{s} = d \ln q / d \ln r$ and $\alpha = -2\mu_0 q^2 L_{\text{ref}} \partial_r \psi p' / B_{\text{ref}}^2$, where L_{ref} is a macroscopic reference length (set by the minor radius a in this work), and B_{ref} is a reference magnetic field (set, here, by the on-axis magnetic field). In total, there are nine shaping parameters. Note that in Ref.⁵², as well as the present work, a modified definition of $s_\kappa = (\kappa - 1)/\kappa$ and $s_\delta = \delta/\sqrt{1 - \delta^2}$ is used. For this work, triangularity is varied $-0.85 \leq \delta \leq 0.85$ from the GA standard case [$r/a = 0.5$, $R_0/a = 3$, $\kappa = 1$, $\delta = 0$, $q = 2$, $\hat{s} = 1$, $\alpha = 0$]⁵⁴. Additionally, $\partial_r R_0$ is fixed at zero.

Visualization of the cross-sections for the circular case and high positive and negative triangularities are provided in Fig. 1. Negative (positive) triangularity has a vertical section on the low (high) field side and a pointed section at the high (low) field side. The changes in the flux surface shapes due to variation of triangularity visualized in Fig. 1 translate to changes in key geometric quantities related to ITG drive and damping.

Understanding the connection between changes in geometric quantities and changes in instability behavior provides a more complete physical description in the role of triangularity in ITG turbulence. Although drift-wave-driven turbulence is well-resolved by the gyrokinetic framework, physical intuition of geometric contributions to ITG damping and drive can be more apparent in fluid-like models. Using a three-field fluid model in Refs.⁵⁵ and⁵⁶, geometric contributions at wavenumber k come from a stabilizing polarization term G_k (see Eqs. (6)–(9)), which considers contributions from the local changes in driving gradients and the local shear, and from a curvature term K_k (see Eqs. (10)–(12)), which may contribute to ITG drive. The polarization term also repre-

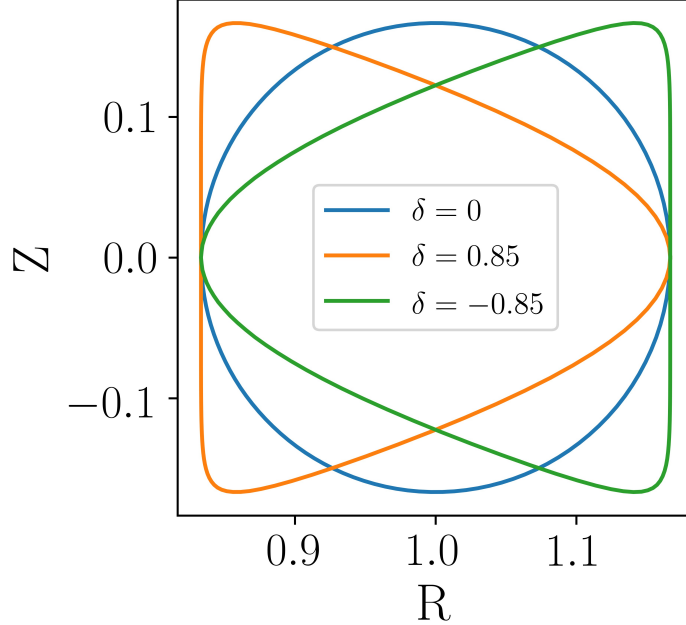


FIG. 1: Cross-sections of flux surfaces for circular ($\delta = 0$, blue), positive triangularity ($\delta = 0.85$, orange), and negative triangularity ($\delta = -0.85$, green) cases plotted in cylindrical coordinates normalized to the major radius of the flux surface, where the toroidal axis is at $R = 0$.

sents the strength of finite-Larmor-radius damping in the Fourier-analyzed gyrokinetic equations. Both G_k and K_k are dimensionless quantities.

Key geometric quantities associated with ITG damping and drive are represented in the present work with local flux-tube geometry as implemented in the GENE code, a massively parallel local and global Vlasov-Maxwell solver used to study microinstabilities and turbulence⁵⁷. In the flux-tube representation employed by GENE, the magnetic field is written as $\mathbf{B}(z) = (d\psi(x)/dx)\nabla x(z) \times \nabla y(z)$, where x is the normalized radial coordinate and y is the normalized binormal coordinate. The coordinate along the magnetic field line is parameterized by $z = \Theta$. The term G_k is stabilizing and associated with the local integrated shear $\Lambda = -\nabla(q\Theta - \zeta) \cdot \nabla\psi/B$:

$$G_k = \theta_k^2 g^{xx} + 2\theta_k g^{xy} + g^{yy}, \quad (6)$$

where $\theta_k = k_x/\hat{s}k_y$. The metric elements are defined by $g^{xx} = \nabla x \cdot \nabla x$, $g^{xy} = \nabla x \cdot \nabla y$, and $g^{yy} =$

$\nabla y \cdot \nabla y$ and are related to the local equilibrium model by

$$g^{xx} = \frac{|\nabla\psi|^2}{(\partial_r\psi)^2}, \quad (7)$$

$$g^{xy} = -\frac{\Lambda B}{B_{\text{ref}}}, \quad (8)$$

$$g^{yy} = \frac{(\partial_r\psi)^2}{B_{\text{ref}}^2} \frac{B^2}{|\nabla\psi|^2} (1 + \Lambda^2). \quad (9)$$

The quantity G_k is a non-negative quantity, where larger values of G_k correspond to increased stabilization. The other geometric quantity of interest is the curvature K_k , which is associated with ITG drive. At zero pressure gradient, K_k is defined as

$$K_k = \theta_k K^x + K^y, \quad (10)$$

$$K^x = -\frac{L_{\text{ref}}}{\partial_r\psi} |\nabla\psi| \kappa_g, \quad (11)$$

$$K^y = \frac{\partial_r\psi L_{\text{ref}}}{B_{\text{ref}}} \frac{B}{|\nabla\psi|} (\kappa_n + \Lambda \kappa_g), \quad (12)$$

where κ_n and κ_g are the normal and geodesic components of the curvature vector $\boldsymbol{\kappa} = \kappa_n \hat{\mathbf{b}} + \kappa_g (\hat{\mathbf{b}} \times \hat{\mathbf{n}})$, with $\hat{\mathbf{b}} = \mathbf{B}/B$ and $\hat{\mathbf{n}} = \nabla\psi/|\nabla\psi|$. The quantity K_k is defined such that $K_k < 0$ (> 0) enhances (reduces) ITG drive.

III. LINEAR INSTABILITY CHARACTERISTICS

The linear gyrokinetic simulations presented in this section are computed through eigenvalue calculations in flux-tube geometry, allowing all linearly unstable modes, dominant or subdominant, to be computed at each (k_x, k_y) wavenumber pair. The ρ_s normalization of the wavenumber will be assumed in the remainder of this work, where $\rho_s = c_s/\Omega_{ci}$ is the ion sound gyroradius, $c_s = \sqrt{T_{i0}/m_i}$, T_{i0} is the background ion temperature, m_i is the ion mass, and Ω_{ci} is the ion gyrofrequency. The ρ_s normalization of the wavenumber will be assumed in the remainder of this work. The electrostatic potential Φ is given in units of $T_{i0}\rho_s/ae$, where e is the elementary charge. Linear growth rates for drift-wave instabilities in tokamaks are commonly analyzed at the radial wavenumber $k_x = 0$ ^{17,22}, under the assumption that the most unstable linear eigenmode occurs at $k_x = 0$, corresponding to highly elongated radial ‘‘streamer’’ structures^{58,59}. The assumption of linear growth rates peaking at $k_x = 0$ does not always hold⁶⁰. Indeed, the present work also finds some positive triangularity configurations that have peak linear growth rates at $k_x \neq 0$.

Growth rates are presented in units of c_s/a and were checked for convergence in the parallel spatial direction by doubling the parallel spatial resolution until growth rates changed by less than

ten percent. The linear simulations use a numerical grid size of $N_x \times N_z \times N_{v_{\parallel}} \times N_{\mu} = 9 \times 32 \times 32 \times 8$, where μ is the magnetic moment. The hyper-diffusion coefficients are $\varepsilon_z = 2$ and $\varepsilon_v = 0.2^{61}$. The normalized temperature and density gradients are $a/L_{Ti} = 4$, $a/L_n = 1$, respectively, and the background temperature ratio is $T_{i0}/T_{e0} = 1$. The background ion temperature gradient was chosen, because, at $a/L_{Ti} = 3$, the nonlinear simulation for $\delta = 0.85$ was in a Dimits regime³⁵. Also, the growth rates scaled with change in a/L_{Ti} indicating the modes were ITG. All simulations, linear and nonlinear, are collisionless and assume $\beta = 0$ with adiabatic electrons. In all cases, ITG is the dominant instability.

III.1. Growth Rate Spectra

First, the dominant linear growth rate spectra for each triangularity are compared. Figure 2 shows the dominant linear growth rate spectra for the circular and negative-triangularity cases. For negative triangularity, the peak growth rates appear at $k_x = 0$, decreasing as δ becomes more negative. Additionally, as δ becomes more negative, the linear growth-rate spectrum broadens as a function of k_x .

However, the positive-triangularity geometries see different trends in the linear growth-rate spectrum, as shown in Fig. 3. The first feature of note is that the peak linear growth rate appears in the range $0.2 \leq k_x \leq 0.35$, increasing in magnitude and shifting to higher k_x for $0.25 \leq \delta \leq 0.75$ before decreasing significantly at $\delta = 0.85$.

Although peak growth rates may increase with positive δ , at low wavenumbers $k_y \lesssim 0.3$, the linear growth rates decrease with δ . Because turbulent transport is typically dominated by modes at low wavenumbers, in many instances, only the $k_x = 0$ modes are considered in linear analysis for tokamaks^{17,22,62}. But, as shown in Fig. 3, the reduced contributions to turbulent transport from growth rates at low (k_x, k_y) may be offset by the contributions from larger growth rates at moderate (k_x, k_y) as triangularity is increased. Additionally, the unstable spectrum substantially narrows in (k_x, k_y) space.

In the geometries $\delta \geq -0.25$, two distinct lobes are observed in the growth-rate spectrum. Cross-phases between Φ and total ion temperature fluctuations, a measure of the efficiency of ITG drive, in each lobe are similar, and all significantly unstable modes are strongly ballooning (strongly peaked at the outboard midplane $z = 0$). The behavior of the different lobes can be attributed to geometric effects, further described in Sec. III.2.

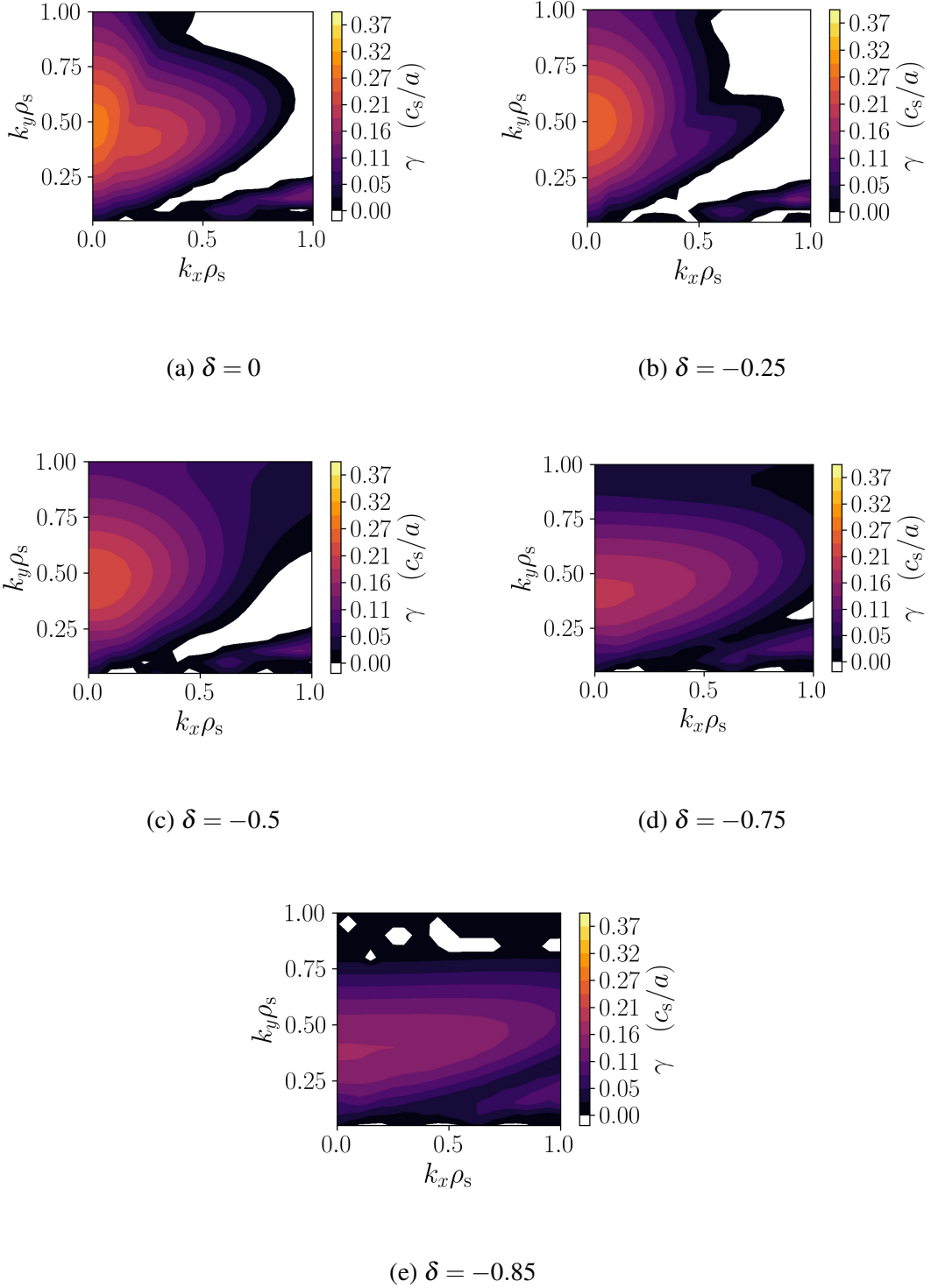


FIG. 2: Growth-rate spectra for $\delta \leq 0$. A fixed color scale is bounded by the largest growth rate for $|\delta| \leq 0.85$. White is a region of stability. Two lobes for $\delta \geq -0.25$ and an island in the lower-right corner of each plot correspond to changes in polarization and curvature terms.

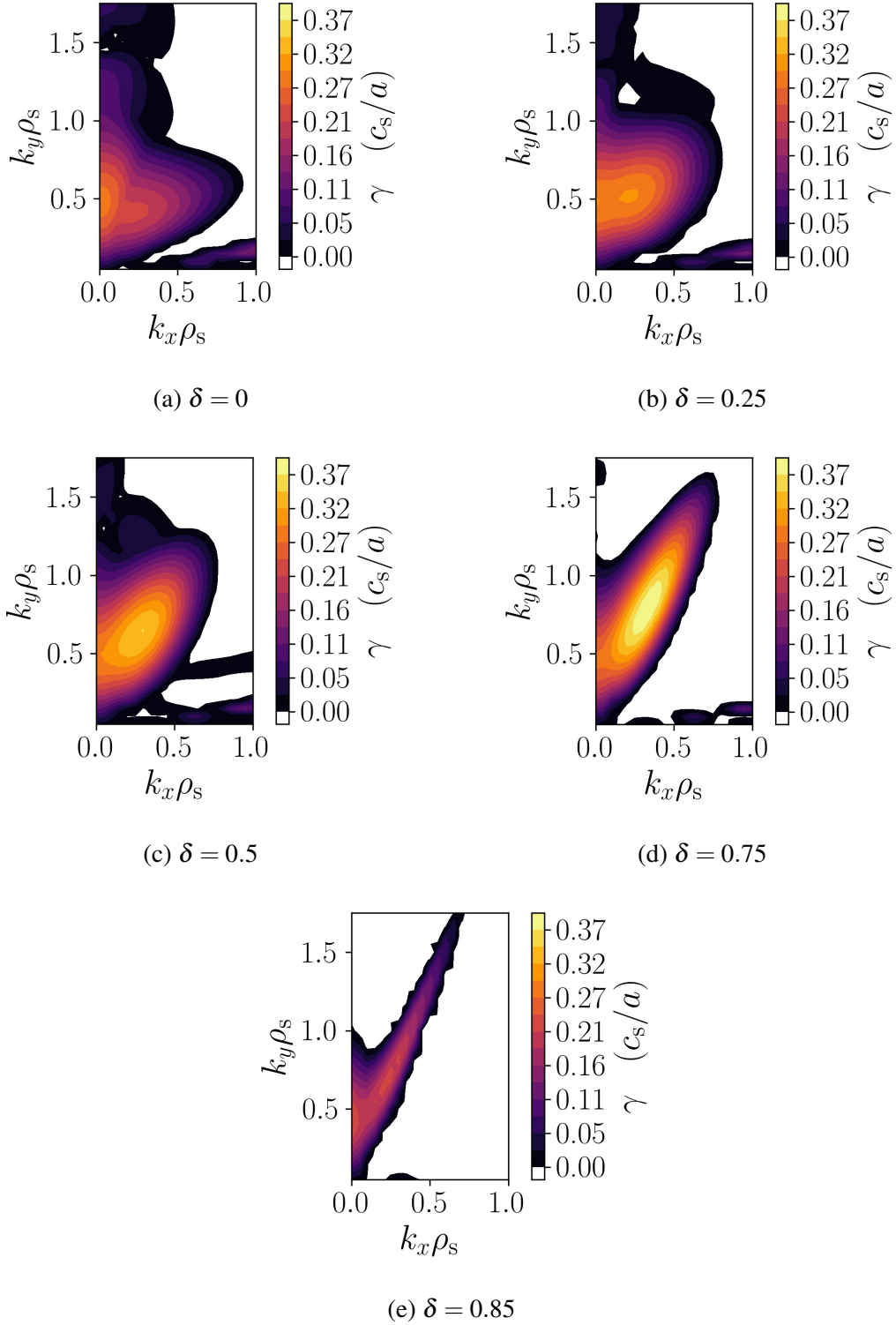


FIG. 3: Growth-rate spectra for $\delta \geq 0$. A fixed color scale is bounded by the largest growth rate for $|\delta| \leq 0.85$. White is a region of stability. Two lobes and an island in the lower-right corner of each plot correspond to changes in polarization and curvature terms.

III.2. Geometric Influences on Linear Growth Rates

To understand how changes in geometry from triangularity affect linear growth rates, the amplitude of the eigenfunctions as a function of the position z along the field line for $(k_x = 0, 0.2, 0.4; k_y = 0.5)$ are plotted with the polarization and curvature terms experienced by the modes in Figs. 4–6. In Fig. 4, for $\delta = 0$, as k_x is increased, the eigenfunction amplitude and polarization term's minimum shifts away from $z = 0$. When the eigenfunction changes shape, it samples a different region of curvature. The change in the shape of the curvature term sampled by the eigenfunction in turn correlates with the transition from one lobe to another in the growth-rate spectrum, which are stabilized due to smaller destabilizing magnitudes of the curvature term. Additionally, the magnitude of the curvature sampled by the eigenfunction correlates well with the change in magnitude of the dominant growth rate. This picture persists in the other geometries as well: the polarization term correlates with the shift in the parallel eigenfunction amplitude profile to a new region of curvature, which correlates with the relative magnitude of the dominant growth rate.

The geometry with $\delta = -0.85$ is used as a representative case for the negative triangularity geometries. In Fig. 5, the polarization and curvature terms are presented with the eigenfunction profile for $\delta = -0.85$. The polarization term forms a large well and is more robust to changes in k_x than the circular case, correlating with the eigenfunction amplitude shifting only slightly away from $z = 0$. The curvature term for negative triangularity is nearly constant about $z = 0$. Although there are regions of strong unfavorable curvature near $z/\pi = 0.5$, only the region of nearly constant curvature is sampled by the eigenfunction of each mode, because of the large amount of shear from the polarization term at the same location along the field line as the only the nearly constant region of curvature centered at $z = 0$. The robustness to changes in k_x of the polarization and curvature terms and of the eigenfunction structure sampling near-constant curvature agree with the increased uniformity in the growth-rate spectrum in k_x in the negative-triangularity geometries.

For $\delta = -0.85$, the upper and lower corners of the flux surface cross-sections shown in Fig. 1 do not correlate strongly with the qualitative trends of the linear growth-rate spectrum. As shown in Fig. 5, local maxima of G_k at $z/\pi = \pm 0.36$ are located near the low field side of the upper and lower corners. In fact, the locations of maximum G_k , which correlates with the width of the eigenfunction, is located on the diagonal edge of the cross-section at $z/\pi = \pm 0.63$ at the point of the most unfavorable curvature.

For positive δ , the geometry with $\delta = 0.85$ is used as a representative. The equivalent data corresponding to that in Figs. 4 and 5 are presented in Fig. 6, but for $\delta = 0.85$. As with $\delta = -0.85$,

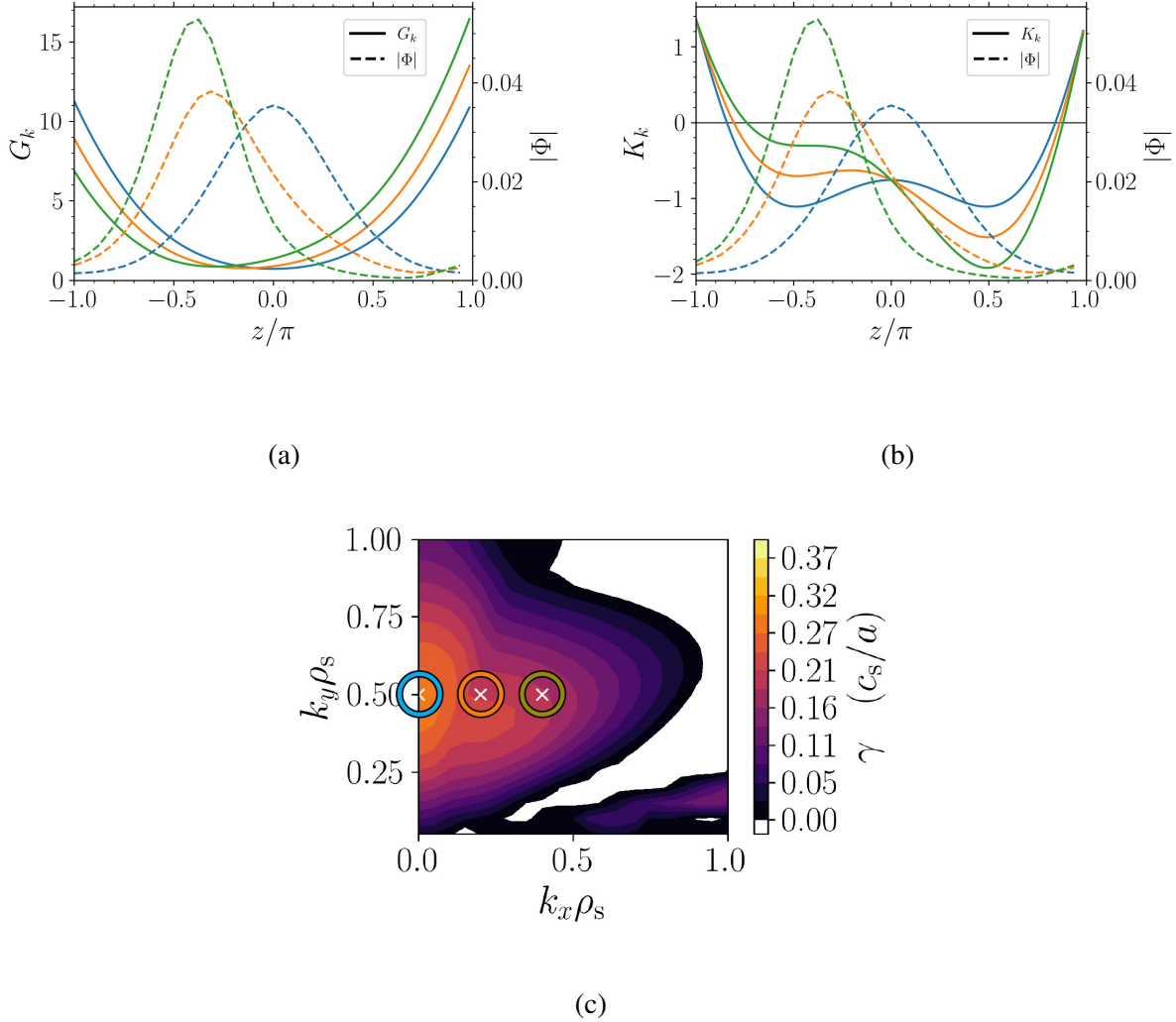


FIG. 4: (a) and (b): Linear eigenfunction amplitudes (dashed lines) as functions of parallel coordinate at $(k_x = 0, 0.2, 0.4; k_y = 0.5)$ (blue, orange, and green, respectively) with polarization (a) and curvature (b) terms (solid lines) for the circular case. The polarization term correlates with the eigenfunction shape, and the less unfavorable magnetic curvature sampled by the eigenfunction as k_x is increased correlates with the decreased magnitude of dominant linear growth rate in the linear growth-rate spectrum (c) at the three modes indicated above. Mode locations in (c) are marked with a white crosses and circles whose colors correspond to the nomenclature in (a) and (b).

a well in the polarization term localizes the eigenfunction along the field line. However, unlike $\delta = -0.85$, the polarization term for the configuration with $\delta = 0.85$ significantly shifts its minimum as k_x is increased, correlating with a significant shift in eigenfunction along the field line. Also,

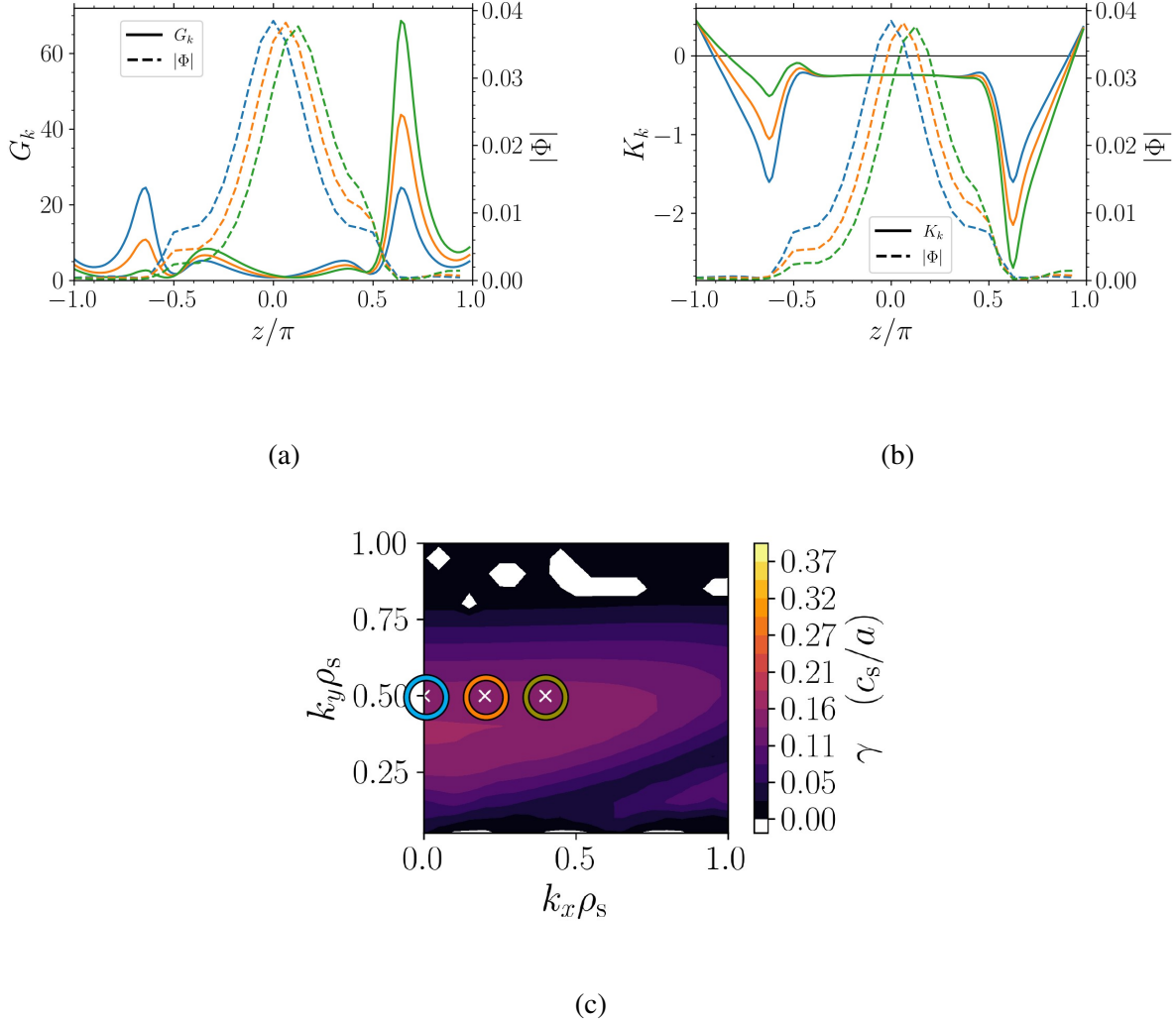


FIG. 5: (a) and (b): Linear eigenfunction amplitudes (dashed lines) as functions of parallel coordinate at $(k_x = 0, 0.2, 0.4; k_y = 0.5)$ (blue, orange, and green, respectively) with polarization (a) and curvature (b) terms (solid lines) for $\delta = -0.85$. The polarization term correlates with the eigenfunction shape, and the similar magnetic curvature sampled by the eigenfunction as k_x is increased correlates with the broadening of the linear growth-rate spectrum (c) as a function of k_x . Mode locations in (c) are marked with a white crosses and circles whose colors correspond to the nomenclature in (a) and (b).

the curvature term has significantly more variation in k_x compared to the $\delta \leq 0$ geometries. For $\delta = 0.85$, the eigenfunction for $(k_x = 0.2, k_y = 0.5)$ is sampling a region of marginally unfavorable curvature, where a small negative (positive) shift in z would (de)stabilize the mode. A negative (positive) shift in z corresponds to a mode with slightly larger (smaller) k_x or k_y . This sensitivity

in wavenumber to curvature sampled by the eigenfunction directly correlates with the observed narrowing of the unstable growth-rate spectrum.

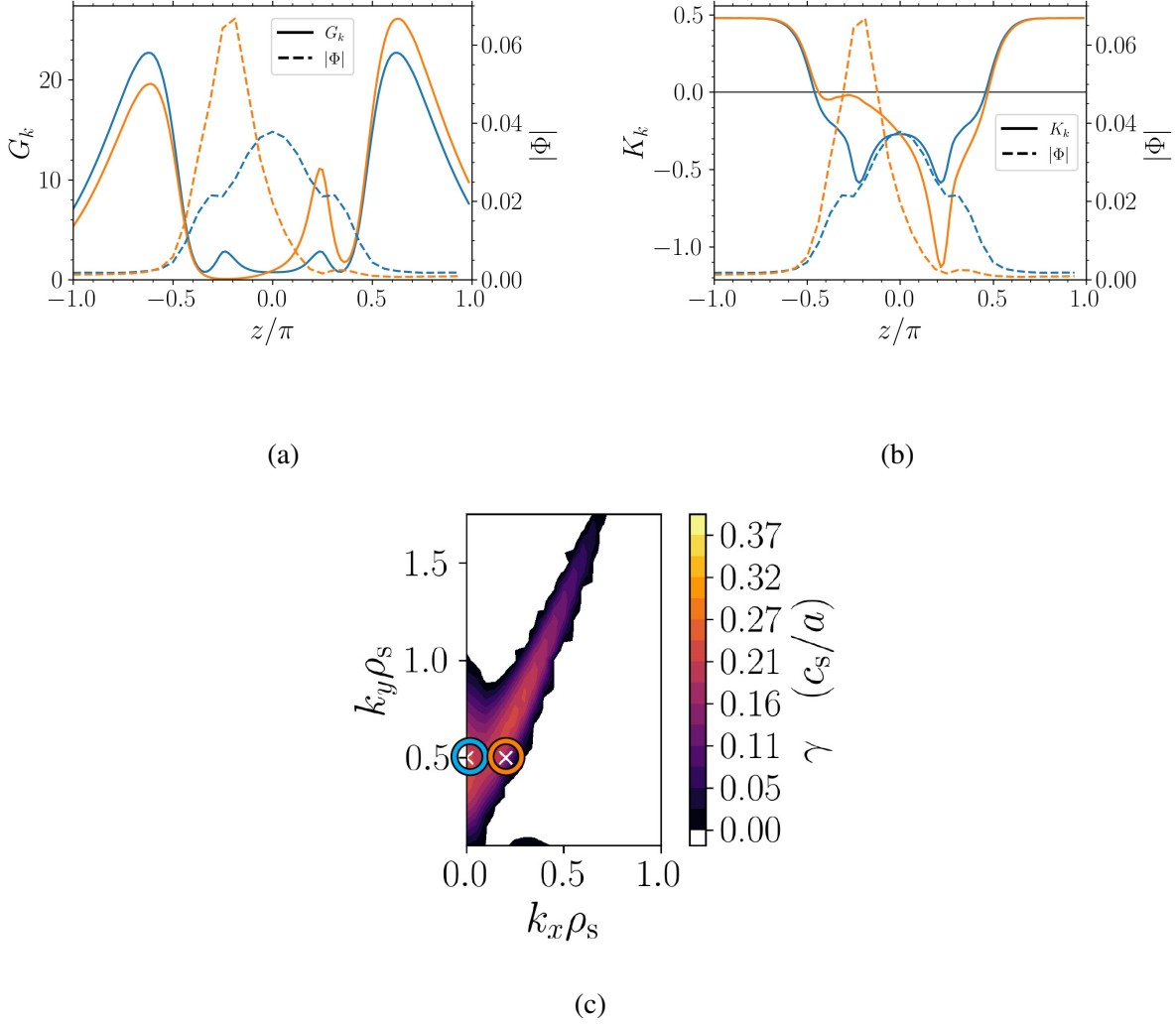


FIG. 6: (a) and (b): Linear eigenfunction amplitudes (dashed lines) as functions of parallel coordinate at $(k_x = 0, 0.2, 0.4; k_y = 0.5)$ (blue and orange, respectively) with polarization (a) and curvature (b) terms (solid lines) for $\delta = 0.85$. The polarization term correlates with the eigenfunction shape, and the magnetic curvature sampled by the eigenfunction as k_x is increased correlates with the narrowing of the linear growth-rate spectrum (c). Mode locations in (c) are marked with a white crosses and circles whose colors correspond to the nomenclature in (a) and (b).

In contrast to $\delta = -0.85$, for $\delta = 0.85$, the upper and lower corners influence qualitative trends of the linear growth-rate spectrum. Here, the maximum values of G_k , as shown in Fig. 6, are on

the high-field side of the upper and lower corners of the flux surface. At finite k_x , one of the global maxima and the local maximum in G_k coinciding with the point lowest K_k correlates with the width of the eigenfunction. However, a change in G_k and K_k with k_x at the flux surface corner does not affect a substantial change in eigenfunction amplitude or curvature sampled. The points along the field line affecting the eigenfunction dependency with k_x and growth spectrum are $z/\pi = \pm 0.2$, which are along the diagonal edges of the cross-section shown in Fig. 1. As k_x is increased, the local maximum in G_k at $z/\pi = 0.2$ is increased, correlating with the change in eigenfunction amplitude. A substantial change in favorability of the curvature with k_x sampled by the eigenfunction occurs at $z/\pi = -0.2$. There, the eigenfunction amplitude is the largest, thus contributing significantly to the growth rate. In summary, the broadening of the growth-rate spectrum in k_x with more negative δ and the narrowing of the growth-rate spectrum with more positive δ and the peak growth rates occurring at $k_x \neq 0$ can be explained by the polarization term localizing the eigenfunction to a region of magnetic curvature, and the upper and lower corners of the flux surface cross-section only influences qualitative trends in the linear growth rate spectrum for $\delta > 0$.

IV. NONLINEAR SIMULATIONS

The properties of linear ITG eigenmodes are insightful and can be used in quasilinear transport models to estimate the relative levels of nonlinear heat fluxes between multiple configurations at a reduced computational cost. However, the quasilinear model is not always predictive^{34,36,37,40,41}, and turbulence is manifestly a nonlinear process. Therefore, it is important to assess the degree of which quasilinear estimates accurately reflect turbulence physics and resultant scalings. Nonlinear simulations are performed with converged grid resolutions $N_x \times N_{k_y} \times N_{v_{\parallel}} \times N_{\mu} = 128 \times 32 \times 48 \times 8$, and $N_z = 32$ for $|\delta| \leq 0.5$ or $N_z = 64$ for $|\delta| \geq 0.75$. Additionally, a radial box size $L_x = 120\rho_s$ and minimum wavenumber simulated $k_y^{\min} = 0.05$ were found to yield numerically converged nonlinear simulations.

Heat fluxes presented in this section have a gyro-Bohm normalization, $Q_{gB} = c_s n_{i0} T_{i0} (\rho_s/a)^2$, where n_{i0} is the background ion density. The time traces of nonlinear heat flux for $\delta = 0$ and $\delta = \pm 0.85$ are plotted in Fig. 7. Reported time averages are taken over the quasistationary state, in all cases covering at least 1000 time units. Nonlinear quantities of interest are obtained by time-averaging over the quasi-stationary state, unless stated otherwise.

The heat fluxes in Fig. 7 are time averaged and decomposed into wavenumbers k_y in Fig. 8. The case $\delta = -0.85$ has a significantly different heat flux spectrum from $\delta = 0$, with two peaks present

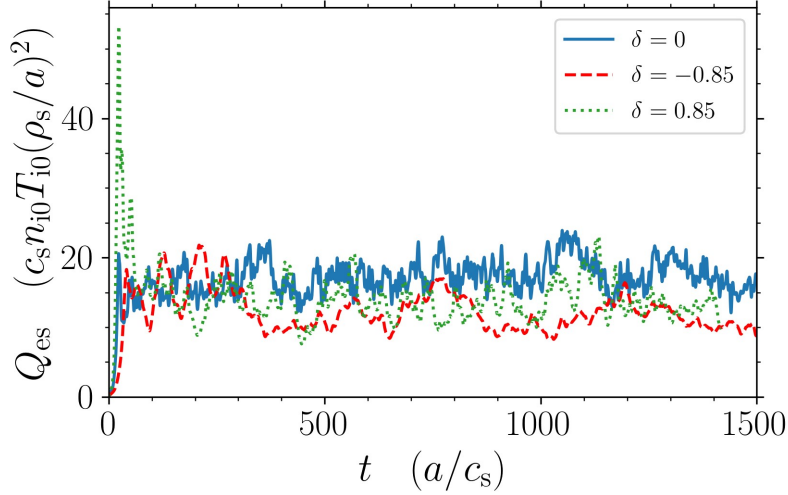


FIG. 7: Time traces of nonlinear electrostatic heat flux for $\delta = 0$ (solid blue), $\delta = -0.85$ (red dashed), and $\delta = 0.85$ (green dotted). By $t = 400a/c_s$, all three plotted cases have reached a quasi-stationary state, where reported nonlinear quantities have been averaged for at least 1000 time units afterward, unless stated otherwise.

at $k_y = 0.05$ and $k_y = 0.2$. At $\delta = 0.85$, a moderate shift of the peaks to $k_y = 0.3$ is observed. Additionally, the upshift in the peak heat flux in k_y implies an upshift in k_x as well, correlating with the shift in peak growth rates to finite k_x for $\delta > 0$.

IV.1. Comparison of Nonlinear and Quasilinear Heat Fluxes

Instead of performing resource-intensive nonlinear gyrokinetic simulations, a quasilinear mixing length argument for the quasilinear heat diffusivity χ^{QL} is sometimes used with linear quantities to estimate nonlinear heat fluxes at much lower computational cost. Beginning from an assumption that the quasilinear heat flux is determined by cross-field diffusive transport due to interacting turbulent eddies with perpendicular spatial scale $\Delta x^2 \propto 1/k_\perp^2$ and time scale $\Delta t \propto 1/\gamma$, Q^{QL} is written as

$$Q^{\text{QL}} = -n\chi^{\text{QL}}\nabla T \quad (13)$$

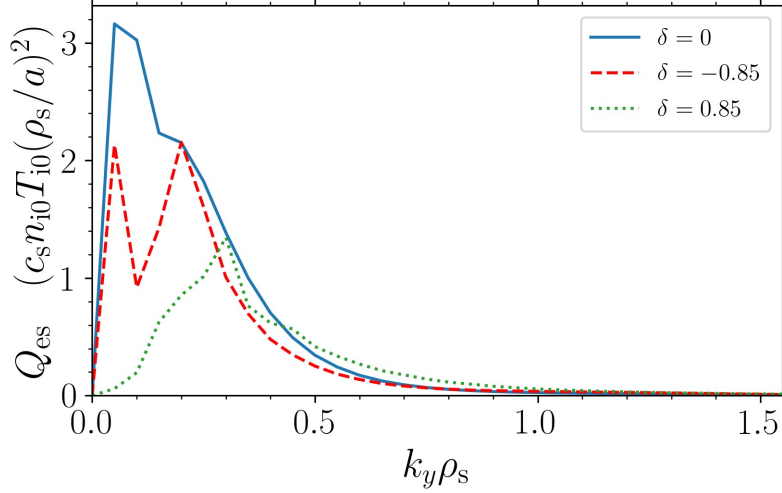


FIG. 8: Heat fluxes as functions of k_y for $\delta = 0$ (solid blue), $\delta = -0.85$ (red dashed), and $\delta = 0.85$ (green dotted). The heat flux spectra are numerically converged, as the heat flux spectra did not appreciably change when k_y^{\min} was halved.

where the quasilinear heat diffusivity is computed by summing over all perpendicular radial and binormal wavenumbers k , with unstable modes indexed by j (see Ref.⁶³)

$$\chi^{\text{QL}} = \mathcal{C} \sum_{k,j} S_k w_{k,j} \frac{\gamma_{k,j}}{\langle k_{\perp,k,j}^2 \rangle}, \quad (14)$$

where

$$\langle k_{\perp,k,j}^2 \rangle = \frac{\int dz [k_x^2 g^{xx} + 2k_x k_y g^{xy} + k_y^2 g^{yy}] \sqrt{g} |\Phi_{k,j}|^2}{\int dz \sqrt{g} |\Phi_{k,j}|^2}, \quad (15)$$

and \sqrt{g} is the Jacobian. In Eqs. (14) and (15), $\Phi_{k,j}$ is the linear eigenfunction, and the weight function is $w_{k,j} = Q_{k,j}/n_{k,j}^2$, where $Q_{k,j}$ and $n_{k,j}^2$ are the linear electrostatic heat flux and perturbed density, respectively. The shape factor S_k weighs each k_y contribution according to a representative nonlinear heat flux spectrum from a reference nonlinear simulation. In the present work, S_k is set by the k_x -integrated nonlinear heat flux spectrum for $\delta = 0$. The constant \mathcal{C} is an overall normalization factor, set here so that the quasilinear and nonlinear integrated heat fluxes for the configuration with $\delta = 0$ match. This is the same model as Ref.⁶³, where Eq. (15) in the present work is equivalent to Eq. (3) in Ref.⁶³ up to a constant factor.

In this work, a quasilinear estimate is initially used to estimate the effect of varying triangularity on turbulent electrostatic (es) ion heat transport. This estimate is subsequently compared with

nonlinear simulation results. The nonlinear heat fluxes Q_{es}^{NL} and quasilinear estimates Q_{es}^{QL} versus δ are presented in Fig. 9. Based on nonlinear heat flux data and statistical uncertainty and finite-resolution effects in turbulence simulations, for $|\delta| \leq 0.5$, nonlinear heat flux has at most a weak dependence on triangularity. However, for $|\delta| = 0.85$, Q_{es}^{NL} decreases strongly. Additionally, the nonlinear heat flux is lower for each value of negative triangularity than it is for the corresponding positive triangularity. These results provide a possible explanation for the equilibrium shaping of an optimized tokamak for ITG turbulence with adiabatic electrons to have substantial negative triangularity²⁵.

Note that most studies reporting improved confinement with negative triangularity were based on TEM or ITG with kinetic electron scenarios at moderate triangularity^{6,9,10,12–18,23}. Specifically, in Refs.^{6,23}, the ITG-dominated regime still had unstable TEMs contributing to the turbulence. Decreasing the electron density gradient would stabilize these TEMs, and the electrons would behave more adiabatically^{24,64}. The inverse relationship of adiabatic behavior of electrons and density gradient combined with the results presented here and in Refs.^{6,23} indicates increasing the density gradient in an ITG-dominated regime with kinetic electrons could make the nonlinear heat flux more sensitive to variations in δ at moderate triangularity.

As shown in Fig. 9, comparing the quasilinear estimates with the nonlinear heat fluxes yields good qualitative agreement for most triangularities. The quasilinear estimates for $|\delta| \leq 0.5$ captured the weak dependence of Q_{es}^{NL} on δ for moderate triangularity. For $|\delta| \geq 0.5$, the quasilinear estimates captures the qualitative decrease of the nonlinear heat fluxes, but the quasilinear estimates for $\delta \geq 0.5$ greatly underestimates the heat flux as a function of triangularity.

Given the importance of zonal flows in toroidal geometry^{35,44,45} (and confirmed in Sec. IV.2), the poor predictive performance of the quasilinear model at strong positive δ could be due to changes in saturation efficiency. Near criticality, however, the quasilinear model used in the present work is expected to overestimate heat fluxes rather than underestimate^{36,37}, suggesting strong triangularity would strongly detune the nonlinear resonance. Detuning of the nonlinear resonance is consistent with strong variation in the linear growth-rate spectrum as a function of k_x (as seen in Fig. 3), as resonant wavenumber triplets involving the zonal flow imply weak k_x variation.

IV.2. Role of Zonal Modes

Because zonal flows play a key role in saturating ITG turbulence in toroidal geometry^{35,44,45}, it is important to understand the behavior and importance of zonal modes, which include zonal

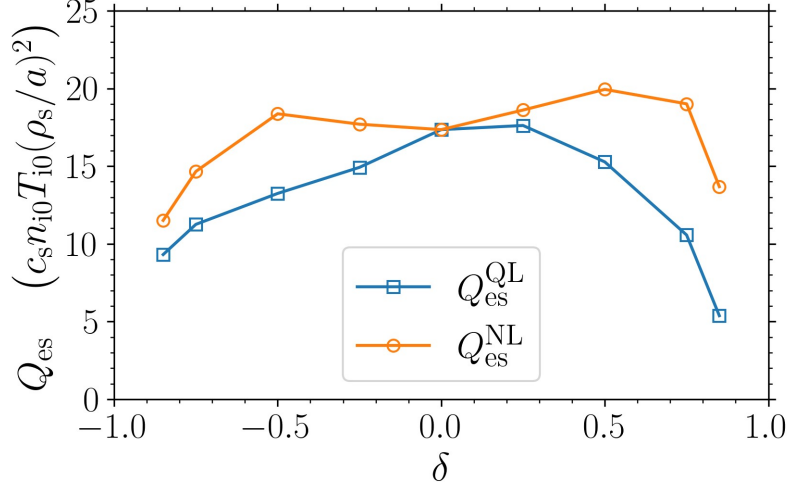


FIG. 9: Nonlinear (orange circles) and quasilinear (blue squares) ion electrostatic heat fluxes in gyro-Bohm units versus triangularity. The quasilinear heat flux is normalized such that the k_x -integrated heat flux spectrum for the circular geometry were equal at each k_y . Nonlinear heat flux is weakly dependent on δ for $|\delta| \leq 0.5$, and decreases strongly for $|\delta| = 0.85$. Quasilinear estimates capture the weak dependence of Q_{es}^{NL} on δ for $|\delta| \leq 0.5$ and substantial decrease for $|\delta| = 0.85$ but overestimates the decrease for $\delta \geq 0.5$.

flows, zonal densities, or zonal temperatures, as triangularity changes. If the zonal $k_y = 0$ mode of the electrostatic potential is removed from a nonlinear gyrokinetic simulation, i.e., $\Phi(k_x, k_y = 0, z) = 0$, which includes the zonal flow $\Phi(k_x, k_y = 0, k_z = 0) = 0$, then the effects of zonal-mediated coupling between unstable and stable modes and zonal-mode damping of nonlinearly transferred energy from an instability are removed from the simulation. Note that while the z direction is not periodic, $k_z = 0$ denotes the z -averaged component. The effect of zeroing out $\Phi(k_x, k_y = 0, z)$ can be quantified by the ratio of nonlinear heat flux without $\Phi(k_x, k_y = 0, z)$ to nonlinear heat flux with $\Phi(k_x, k_y = 0, z)$ retained. A ratio greater than one indicates $\Phi(k_x, k_y = 0, z)$ contribute to lowering the saturated heat flux levels in nonlinear gyrokinetic simulations. If one configuration has a larger ratio of heat fluxes than another, then $\Phi(k_x, k_y = 0, z)$ contributes more in the saturation of turbulence in that configuration.

This procedure was applied in nonlinear simulations by setting the value of $\Phi(k_x, k_y = 0, z) = 0$ at each simulation time step. Hereafter, this scenario is referred to as zonal-mode-suppressed

(ZMS). The ratio of ZMS nonlinear heat fluxes to $Q_{\text{es}}^{\text{NL}}$ is plotted in Fig. 10. For $\delta = -0.25$ and $\delta = -0.5$, following this prescription results in turbulence with numerically poorly-conditioned behavior, such as large local gradients on radial scales comparable to the grid spacing. Thus, data for these particular δ is omitted from the figure. For all other geometries, removing the zonal flows increased the nonlinear heat flux significantly, indicating zonal modes play an important role in turbulent saturation for all geometries studied. As shown in Fig. 10, at positive triangularities, the ratios were larger, with the general trend of more positive triangularity having a larger ratio of ZMS to original heat fluxes, which in turn suggests zonal flows are more important for turbulent saturation as positive δ is increased. The ratios of ZMS to original heat flux are only three percent lower than the circular case for $\delta = -0.85$ and about 25% lower for $\delta = -0.75$, suggesting zonal flows are relatively less important for turbulent saturation than they are in the case of the circular and positive-triangularity geometries.

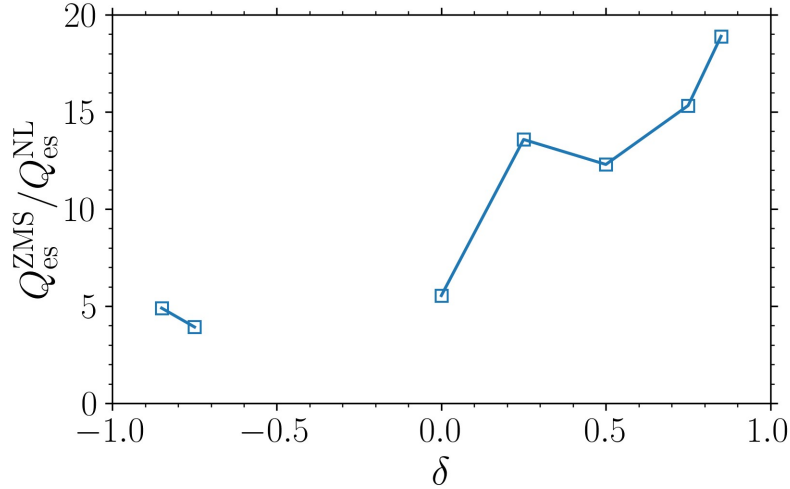


FIG. 10: The ratio of nonlinear electrostatic heat flux where $\Phi(k_x, k_y = 0, z)$ was artificially suppressed at each time step to that of the original, at each triangularity.

The relative enhancement of zonal flows due to changes in triangularity is estimated using the zonal-flow residual $|\Phi_Z|(t \rightarrow \infty)/|\Phi_Z|(t = 0)$ as a proxy for zonal-flow damping⁶⁵ (although in axisymmetric geometry this is not a dissipative process in the absence of collisions) and a k_{\perp}^2 average of the nonlinear fluctuation spectrum summed over non-zonal wavenumbers in Eq. (15), with the nonlinear eigenfunction as a proxy for zonal flow drive. Physically, the zonal-flow residual is a

measure of the bounce-averaged linear response to an externally applied electrostatic potential and is a function of magnetic geometry. Once an instantaneous electrostatic potential is applied, the part of the potential associated with geodesic acoustic modes decays, leaving an undamped component of the potential, which is the zonal-flow residual. The zonal-flow residual is an inverse proxy for zonal-flow damping, because a larger zonal-flow residual indicates less damping of the zonal flow. Prior studies have shown that zonal residuals increase with increasing positive triangularity^{22,66}. The non-zonal spectrally averaged value of k_{\perp}^2 is a proxy for zonal-flow drive for two reasons. It is a measure of energy available for zonal flows from the turbulence spectrum^{46–50,56}. It also quantifies the strength of the nonlinearity that drives flows, which is given by the advection of vorticity. As such, the advection of vorticity nonlinearity has a factor of k_{\perp}^2 relative to other nonlinearities. A larger non-zonal energy average and zonal-flow residual indicate that zonal flows are enhanced, because the drive mechanism for zonal flows from the non-zonal energy spectrum is larger and a larger fraction of the potential is undamped, respectively.

In Fig. 11, the proxies for zonal-flow damping and drive are plotted. In the present work, the zonal residual is computed at $k_x = 0.05$, which is representative of zonal flows at length scales relevant to ITG saturation physics⁴¹ and the k_x -dependence of the zonal residual is very weak at these length scales⁶⁷. For positive triangularity, the zonal residual increases, indicating less zonal-flow damping with increasing positive δ . Although elongation of the flux surfaces in the present work are not the same as Refs.^{22,66}, the trend in zonal residuals for moderate positive triangularity is in agreement with Refs.^{22,66}. Larger zonal-flow residuals and more nonlinear drive indicate enhanced zonal flows in positive triangularity, in agreement with nonlinear data. For $\delta = -0.25$, and $\delta = -0.5$, there is both more damping and drive, making it difficult to conclude the relative role of zonal flows compared with $\delta \geq 0$. For $\delta \leq -0.75$, there is marginally less drive and slightly more damping, indicating zonal flows may be somewhat diminished compared to zonal flows for $\delta \geq 0$. The relative increase of non-zonal energy over zonal-flow residual in $\delta \leq 0$ suggests non-zonal nonlinear interactions may play a larger role in saturating ITG turbulence at those geometries, correlating well with the data in Fig. 10. However, given the findings from Fig. 10, zonal flows remain the primary saturation mechanisms, even at $\delta \leq -0.75$.

V. CONCLUSIONS

A linear and nonlinear electrostatic gyrokinetic study of ITG turbulence with adiabatic electrons has been conducted varying triangularity while holding other shaping parameters of the Miller

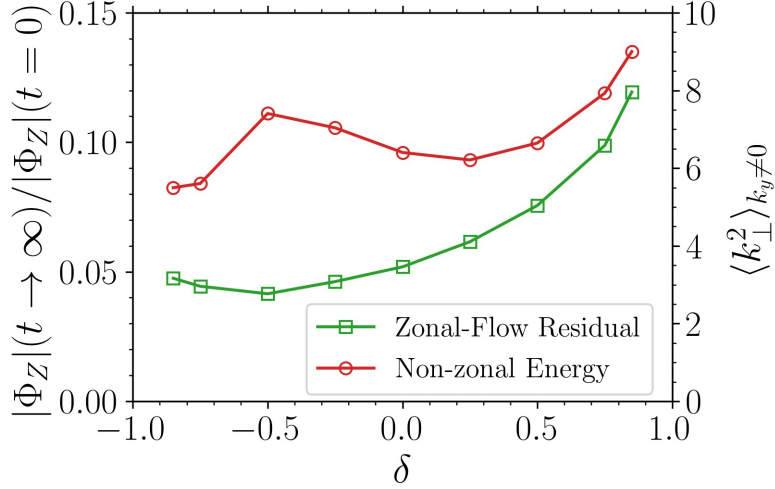


FIG. 11: Zonal-flow residuals (green squares, left axis) and nonlinear non-zonal energy (red circles, right axis) versus triangularity. The zonal-flow residual acts as a proxy for linear damping of zonal flows (larger residual means less damping), and the non-zonal energy is a proxy for zonal-flow drive. Both larger (smaller) zonal-flow residuals and non-zonal energy suggest zonal flows are enhanced (diminished) for $\delta \geq 0$ ($\delta \leq -0.75$).

equilibrium⁵² fixed. Linear simulations show that as triangularity becomes more negative, the maximum growth rate decreases, and the growth-rate spectrum broadens as a function of k_x . As triangularity becomes more positive, the peak growth rate increases and shifts to finite k_x before decreasing at $\delta = 0.85$. Also, the growth-rate spectrum narrows substantially in k_x and k_y with more positive triangularity.

These changes in linear behavior are explained by changes in the polarization term G_k and curvature term K_k , as defined in Eqs. (6)–(12), where the polarization term influences the parallel structure and localization of the linear eigenmode, which samples different regions of favorable or unfavorable curvature, setting the growth rate accordingly. While both terms influence the shape of the linear eigenfunction as a function of magnetic field line coordinate, the polarization term correlates strongly with the change in eigenfunction shape with perpendicular wavenumber. Negative-triangularity geometries have polarization terms and parallel eigenmode profiles that are more robust to changes in k_x , and is not substantially affected by the upper and lower corners of the flux surface cross-section. For positive-triangularity geometries, the polarization term and

parallel eigenmode profile are more sensitive to changes in k_x as eigenmodes shift to regions of more favorable curvature, correlating well with the narrowing of the growth-rate spectrum, and is partially affected by the upper and lower corners of the flux surface cross-section.

A quasilinear transport model is compared to time-averaged quasi-stationary nonlinear electrostatic heat fluxes. Both quasilinear estimates and nonlinear heat fluxes show qualitative agreement, where the heat flux has a weak dependence on triangularity for $|\delta| = 0.5$, decreasing significantly when $|\delta| \geq 0.75$. Additionally, at $|\delta| \geq 0.75$, the negative-triangularity equilibrium has a lower nonlinear heat flux than the corresponding positive triangularity geometry, which is not captured by the quasilinear estimates. For the present case, triangularity, while favorable for improving confinement, produces no large changes in the heat flux except for the highest values of $|\delta|$, indicating negative triangularity is marginally more favorable for reducing ITG-driven turbulence. Prior studies on negative triangularity concluded improved confinement resulted from reductions in TEM turbulence in ITG-dominant regimes with strong enough density gradients for TEM destabilization and in TEM-dominant regimes^{6,9,10,12–18,23}. This phenomenon is not observed here as only adiabatic electrons were employed to isolate ITG physics.

The importance of zonal flows in turbulence saturation was studied via nonlinear simulations artificially suppressing $\Phi(k_x, k_y = 0, z)$, and by assessing the relative strength of zonal flows using the proxies zonal-flow residuals⁶⁵ for the zonal-flow damping and $\langle k_\perp^2 \rangle$ for the nonlinear zonal-flow drive. When removing $\Phi(k_x, k_y = 0, z)$, the nonlinear heat fluxes increase by at least a factor of four compared to the unmodified simulations, indicating zonal flows play an important role in saturating ITG turbulence in each configuration studied in the present work. Positive triangularities have a larger ratio of nonlinear heat flux with suppression to nonlinear heat flux without relative to the circular case, and negative triangularities have a slightly lower ratio, meaning zonal flows play a larger role in saturating ITG turbulence at larger triangularities. An increase in zonal-flow residuals and the nonlinear non-zonal energy indicates zonal flows are indeed expected to be stronger as positive triangularity increased. For strongly-negative-triangularity equilibria, the zonal-flow residuals decrease marginally along with the nonlinear non-zonal energy, suggesting zonal flows are expected to be weaker at negative triangularity.

Together, these results indicate that, in the electrostatic regime with adiabatic electrons studied here, moderate negative values of triangularity have only a modest beneficial effect on reducing heat transport from ITG turbulence, while extreme values of triangularity, both negative and positive, have a substantial beneficial affect. The importance of zonal flows in the geometries studied combined with the quasilinear model underestimating the heat flux near criticality for strong posi-

tive δ , suggests triangularity changes saturation efficiency. The observed improvements associated with negative triangularity seen in experiments likely involve combinations of other aspects of the MHD equilibrium and the associated axisymmetric shaping impacting other microinstabilities, kinetic electrons, plasma β , and temperature and density gradients.

ACKNOWLEDGMENTS

This work is supported by the US Department of Energy, Office of Science, Fusion Energy Services under grants nos. DE-FG02-86ER53218, DE-FG02-99ER54546, DE-FG02-93ER54222, DE-FG02-89ER53291, DE-FG02-93ER54222, and DE-AR0001287 and by the EUROfusion – Theory and Advanced Simulation Coordination (E-TASC). This work has been carried out within the framework of the EUROfusion Consortium and has received funding from the Euratom research and training program 2014-2018 and 2019-2020 under grant agreement no. 633053. The views and opinions expressed herein do not necessarily reflect those of the European Commission. Computing resources were provided through the National Energy Research Scientific Computing Center, a DOE Office of Science User Facility, grant no. DE-AC02-05CH11231.

DATA AVAILABILITY

The data that support the findings of this study are available from the corresponding author upon reasonable request.

REFERENCES

- ¹P. C. Liewer, Nucl. Fusion **25**, 543 (1985).
- ²R. J. Buttery, B. Covele, J. Ferron, A. Garofalo, C. T. Holcomb, T. Leonard, J. M. Park, T. Petrie, C. Petty, G. Staebler, E. J. Strait, and M. Van Zeeland, J. Fusion Energy **38**, 72 (2019).
- ³L. I. Rudakov and R. Z. Sagdeev, Dokl. Akad. Nauk SSR **138**, 581 (1961).
- ⁴W. Horton, D.-I. Choi, and W. M. Tang, Phys. Fluids **24**, 1077 (1981).
- ⁵B. B. Kadomtsev and O. P. Pogutse, Nucl. Fusion **11**, 67 (1971).
- ⁶J. E. Kinsey, R. E. Waltz, and J. Candy, Phys. Plasmas **14**, 102306 (2007).
- ⁷P. Angelino, X. Garbet, L. Villard, A. Bottino, S. Jolliet, P. Ghendrih, V. Grandgirard, B. F. McMillan, Y. Sarazin, G. Dif-Pradalier, and T. M. Tran, Phys. Rev. Lett. **102**, 195002 (2009).

- ⁸O. Beeke, M. Barnes, M. Romanelli, M. Nakata, and M. Yoshida, *Nucl. Fusion* **61**, 066020 (2021).
- ⁹H. Weisen, J.-M. Moret, S. Franke, I. Furno, Y. Martin, M. Anton, R. Behn, M. J. Dutch, B. P. Duval, F. Hofmann, B. Joye, C. Nieswand, Z. A. Pietrzyk, and W. V. Toledo, *Nucl. Fusion* **37**, 1741 (1997).
- ¹⁰J.-M. Moret, S. Franke, H. Weisen, M. Anton, R. Behn, B. P. Duval, F. Hofmann, B. Joye, Y. Martin, C. Nieswand, Z. A. Pietrzyk, and W. van Toledo, *Phys. Rev. Lett.* **79**, 2057 (1997).
- ¹¹A. Pochelon, T. Goodman, M. Henderson, C. Angioni, R. Behn, S. Coda, F. Hofmann, J.-P. Hogge, N. Kirneva, A. Martynov, J.-M. Moret, Z. Pietrzyk, F. Porcelli, H. Reimerdes, J. Rommers, E. Rossi, O. Sauter, M. Tran, H. Weisen, S. Alberti, S. Barry, P. Blanchard, P. Bosshard, R. Chavan, B. Duval, Y. Esipchuck, D. Fasel, A. Favre, S. Franke, I. Furno, P. Gorgerat, P.-F. Isoz, B. Joye, J. Lister, X. Llobet, J.-C. Magnin, P. Mandrin, A. Manini, B. Marlétaz, P. Marmillod, Y. Martin, J.-M. Mayor, J. Mlynar, C. Nieswand, P. Paris, A. Perez, R. Pitts, K. Razumova, A. Refke, E. Scavino, A. Sushkov, G. Tonetti, F. Troyon, W. V. Toledo, and P. Vyas, *Nucl. Fusion* **39**, 1807 (1999).
- ¹²M. Fontana, L. Porte, S. Coda, O. Sauter, and TCV Team, *Nucl. Fusion* **58**, 024002 (2018).
- ¹³M. E. Austin, A. Marinoni, M. L. Walker, M. W. Brookman, J. S. deGrassie, A. W. Hyatt, G. R. McKee, C. Petty, T. Rhodes, S. P. Smith, C. Sung, K. E. Thome, and A. D. Turnbull, *Phys. Rev. Lett.* **122**, 115001 (2019).
- ¹⁴A. Marinoni, M. E. Austin, A. W. Hyatt, M. L. Walker, J. Candy, C. Chrystal, C. J. Lasnier, G. R. McKee, T. Odstreil, C. C. Petty, M. Porkolab, J. C. Rost, O. Sauter, S. P. Smith, G. M. Staebler, C. Sung, K. E. Thome, A. D. Turnbull, L. Zeng, and DIII-D Team, *Phys. Plasmas* **26**, 042515 (2019).
- ¹⁵A. J. Brizard and T. S. Hahm, *Rev. Mod. Phys.* **79**, 421 (2007).
- ¹⁶Y. Camenen, A. Pochelon, R. Behn, A. Bottino, A. Bortolon, S. Coda, A. Karpushov, O. Sauter, G. Zhuang, and TCV team, *Nucl. Fusion* **47**, 510 (2007).
- ¹⁷A. Marinoni, S. Brunner, Y. Camenen, S. Coda, J. P. Graves, X. Lapillonne, A. Pochelon, O. Sauter, and L. Villard, *Plasma Phys. Control. Fusion* **51**, 055016 (2009).
- ¹⁸G. Merlo, S. Brunner, O. Sauter, Y. Camenen, T. Görler, F. Jenko, A. Marinoni, D. Told, and L. Villard, *Plasma Phys. Control. Fusion* **57**, 054010 (2015).
- ¹⁹G. Merlo, Z. Huang, C. Marini, S. Brunner, S. Coda, D. Hatch, D. Jarema, F. Jenko, O. Sauter, and L. Villard, *Plasma Phys. Control. Fusion* **63**, 044001 (2021).

- ²⁰M. Kikuchi, T. Takizuka, and M. Furukawa, in *Proceedings of the 12th Asia Pacific Physics Conference (APPC12)* (Journal of the Physical Society of Japan, Makuhari, Japan, 2014).
- ²¹A. Pochelon, P. Angelino, R. Behn, S. Brunner, S. Coda, N. Kirneva, S. Y. Medvedev, H. Reimerdes, J. Rossel, O. Sauter, L. Villard, D. Wágner, A. Bottino, Y. Camenen, G. P. Canal, P. K. Chattopadhyay, B. P. Duval, A. Fasoli, T. P. Goodman, S. Jolliet, A. Karpushov, B. Labit, A. Marinoni, J.-M. Moret, A. Pitzschke, L. Porte, M. Rancic, V. S. Udintsev, and the TCV Team, *Plasma Fusion Res.* **7**, 2502148 (2012).
- ²²E. A. Belli, G. W. Hammett, and W. Dorland, *Phys. Plasmas* **15**, 092303 (2008).
- ²³G. Merlo, M. Fontana, S. Coda, D. Hatch, S. Janhunen, L. Porte, and F. Jenko, *Phys. Plasmas* **26**, 102302 (2019).
- ²⁴M. Kotschenreuther, X. Liu, D. R. Hatch, S. M. Mahajan, M. J. Pueschel, M. Halfmoon, M. Zarnsdorf, A. Garofalo, J. McClenaghan, I. J. McKinney, J. Qian, S. Ding, C. Giroud, J. C. Hillesheim, C. F. Maggi, S. Saarelma, X. Chen, JET Collaborators Team, and DIII-D Team, in *APS Division of Plasma Physics Meeting Abstracts*, APS Meeting Abstracts, Vol. 2020 (2020) p. VP14.017.
- ²⁵E. G. Highcock, N. R. Mandell, M. Barnes, and W. Dorland, *J. Plasma Phys.* **84**, 905840208 (2018).
- ²⁶A. Kendl and B. D. Scott, *Phys. Plasmas* **13**, 012504 (2006).
- ²⁷J. W. Connor, R. J. Hastie, and J. B. Taylor, *Phys. Rev. Lett.* **40**, 396 (1978).
- ²⁸R. L. Dewar and A. H. Glasser, *Phys. Fluids* **26**, 3038 (1983).
- ²⁹M. Kotschenreuther, W. Dorland, M. A. Beer, and G. W. Hammett, *Phys. Plasmas* **2**, 2381 (1995).
- ³⁰R. E. Waltz, G. M. Staebler, W. Dorland, G. W. Hammett, M. Kotschenreuther, and J. A. Konings, *Phys. Plasmas* **4**, 2482 (1997).
- ³¹F. Jenko, T. Dannert, and C. Angioni, *Plasma Phys. Control. Fusion* **47**, B195 (2005).
- ³²J. E. Kinsey, G. M. Staebler, and R. E. Waltz, *Phys. Plasmas* **15**, 055908 (2008).
- ³³A. Casati, C. Bourdelle, X. Garbet, F. Imbeaux, J. Candy, F. Clairet, G. Dif-Pradalier, G. Falchetto, T. Gerbaud, V. Grandgirard, Ö. Gürçan, P. Hennequin, J. Kinsey, M. Ottaviani, R. Sabot, Y. Sarazin, L. Vermare, and R. E. Waltz, *Nucl. Fusion* **49**, 085012 (2009).
- ³⁴I. J. McKinney, M. J. Pueschel, B. J. Faber, C. C. Hegna, J. N. Talmadge, D. T. Anderson, H. E. Mynick, and P. Xanthopoulos, *J. Plasma Phys.* **85**, 905850503 (2019).
- ³⁵A. M. Dimits, B. I. Cohen, N. Mattor, W. M. Nevins, D. E. Shumaker, S. E. Parker, and C. Kim, *Nucl. Fusion* **40**, 661 (2000).
- ³⁶M. Pueschel, P.-Y. Li, and P. Terry, *Nucl. Fusion* **61**, 054003 (2021).

- ³⁷P. W. Terry, P.-Y. Li, M. J. Pueschel, and G. G. Whelan, *Phys. Rev. Lett.* **126**, 025004 (2021).
- ³⁸M. J. Pueschel, M. Kammerer, and F. Jenko, *Phys. Plasmas* **15**, 102310 (2008).
- ³⁹M. J. Pueschel and F. Jenko, *Phys. Plasmas* **17**, 062307 (2010).
- ⁴⁰G. G. Whelan, M. J. Pueschel, and P. W. Terry, *Phys. Rev. Lett.* **120**, 175002 (2018).
- ⁴¹G. G. Whelan, M. J. Pueschel, P. W. Terry, J. Citrin, I. J. McKinney, W. Guttenfelder, and H. Dörner, *Phys. Plasmas* **26**, 082302 (2019).
- ⁴²G. W. Hammett, M. A. Beer, W. Dorland, S. C. Cowley, and S. A. Smith, *Plasma Phys. Control. Fusion* **35**, 973 (1993).
- ⁴³W. Horton, *Rev. Mod. Phys.* **71**, 735 (1999).
- ⁴⁴P. H. Diamond, S.-I. Itoh, K. Itoh, and T. S. Hahm, *Plasma Phys. Control. Fusion* **47**, R35 (2005).
- ⁴⁵P. W. Terry, *Rev. Mod. Phys.* **72**, 109 (2000).
- ⁴⁶P. W. Terry, D. A. Baver, and S. Gupta, *Phys. Plasmas* **13**, 022307 (2006).
- ⁴⁷D. R. Hatch, P. W. Terry, W. M. Nevins, and W. Dorland, *Phys. Plasmas* **16**, 022311 (2009).
- ⁴⁸D. R. Hatch, P. W. Terry, F. Jenko, F. Merz, M. J. Pueschel, W. M. Nevins, and E. Wang, *Phys. Plasmas* **18**, 055706 (2011).
- ⁴⁹D. R. Hatch, P. W. Terry, F. Jenko, F. Merz, and W. M. Nevins, *Phys. Rev. Lett.* **106**, 115003 (2011).
- ⁵⁰K. D. Makwana, P. W. Terry, and J.-H. Kim, *Phys. Plasmas* **19**, 062310 (2012).
- ⁵¹P. W. Terry, K. D. Makwana, M. J. Pueschel, D. R. Hatch, F. Jenko, and F. Merz, *Phys. Plasmas* **21**, 122303 (2014).
- ⁵²R. L. Miller, M. S. Chu, J. M. Greene, Y. R. Lin-Liu, and R. E. Waltz, *Phys. Plasmas* **5**, 973 (1998).
- ⁵³C. C. Hegna, *Phys. Plasmas* **7**, 3921 (2000).
- ⁵⁴R. E. Waltz and R. L. Miller, *Phys. Plasmas* **6**, 4265 (1999).
- ⁵⁵J. Anderson, T. Rafiq, M. Nadeem, and M. Persson, *Phys. Plasmas* **9**, 1629 (2002).
- ⁵⁶C. C. Hegna, P. W. Terry, and B. J. Faber, *Phys. Plasmas* **25**, 022511 (2018).
- ⁵⁷F. Jenko, *Comput. Phys. Commun.* **125**, 196 (2000).
- ⁵⁸J. F. Drake, P. N. Guzdar, and A. B. Hassam, *Phys. Rev. Lett.* **61**, 2205 (1988).
- ⁵⁹F. Jenko, W. Dorland, M. Kotschenreuther, and B. N. Rogers, *Phys. Plasmas* **7**, 1904 (2000).
- ⁶⁰D. Told, F. Jenko, P. Xanthopoulos, L. D. Horton, E. Wolfrum, and A. U. Team, *Phys. Plasmas* **15**, 102306 (2008).
- ⁶¹M. J. Pueschel, T. Dannert, and F. Jenko, *Comput. Phys. Commun.* **181**, 1428 (2010).

- ⁶²M. J. Pueschel, D. R. Hatch, D. R. Ernst, W. Guttenfelder, P. W. Terry, J. Citrin, and J. W. Connor, *Plasma Phys. Control. Fusion* **61**, 034002 (2019).
- ⁶³M. J. Pueschel, B. J. Faber, J. Citrin, C. C. Hegna, P. W. Terry, and D. R. Hatch, *Phys. Rev. Lett.* **116**, 085001 (2016).
- ⁶⁴F. Romanelli and S. Briguglio, *Physics of Fluids B: Plasma Physics* **2**, 754 (1990).
- ⁶⁵M. N. Rosenbluth and F. L. Hinton, *Phys. Rev. Lett.* **80**, 724 (1998).
- ⁶⁶Y. Xiao and P. J. Catto, *Phys. Plasmas* **13**, 082307 (2006).
- ⁶⁷P. Monreal, I. Calvo, E. Sánchez, F. I. Parra, A. Bustos, A. Könies, R. Kleiber, and T. Görler, *Plasma Phys. Control. Fusion* **58**, 045018 (2016).